Materials Advances

ROYAL SOCIETY OF CHEMISTRY

PAPER

View Article Online
View Journal | View Issue

Cite this: *Mater. Adv.*, 2025, 6, 8023

Leveraging TIPS-assisted one-pot di-bromination for thiazole-flanked NDI and PDI conjugated n-type semiconductors

Salahuddin S. Attar, †[a] Ji Hwan Kim, †[b] Maciej Barłóg,[a] Dusan Sredojevic,[c] Alex Kalin,[d] Lei Fang,[d] Hassan S. Bazzi,[e] Sara J. Al-Hail,[f] Myung-Han Yoon[b] and Mohammed Al-Hashimi *[e]

Received 1st June 2025,
Accepted 29th September 2025

DOI: 10.1039/d5ma00573f

rsc.li/materials-advances

High-performance unipolar n-type semiconductors are essential for advancing organic electronics. This study explores the impact of fluorination on thiazole-flanked naphthalenediimide (NDI) and perylenediimide (PDI) copolymers with benzothiadiazole (BT) acceptors. A novel one-pot bromination strategy enabled efficient synthesis of these electron-deficient monomers, which were subsequently copolymerized with fluorinated and non-fluorinated BT units. Optical and electrochemical analyses revealed that fluorination systematically lowers the LUMO energy levels, enhancing charge injection and n-type behavior. Fluorine substitution also influences molecular packing, as evidenced by UV-Vis absorption shifts, cyclic voltammetry, and grazing-incidence wide-angle X-ray scattering (GIWAXS). While moderate fluorination improves electron mobility by promoting backbone planarity and π–π stacking, excessive substitution disrupts molecular ordering, reducing charge transport efficiency. The optimized fluorinated copolymers exhibit electron mobilities up to 1.3 × 10^{-3} cm^2 V^{-1} s^{-1}, demonstrating the potential of fluorination in tuning electronic properties for next-generation hybrid organic semiconductors.

Introduction

Electron-transporting (n-type) conjugated polymers are essential for advancing organic electronic devices, like organic field-effect transistors (OFETs), electrochemical transistors (OECTs), solar cells, thermoelectric materials and sensors.[1–7] However, achieving high-performance n-type materials remains challenging due to the need of high electron affinity, efficient intermolecular electronic orbital overlap for enhanced mobility, and air stability.[8–12] One promising strategy to enhance mobility in n-type materials is the incorporation of diverse acceptor units, particularly A–A-type (double acceptor) copolymers.[13] These copolymers exhibit strong electron-withdrawing characteristics, making them highly promising, by combining different acceptor units, researchers have been able to develop new n-type materials with enhanced electronic properties. Notably, A–A-type polymer-based OFETs have achieved exceptional electron mobility (μ_e), with recent values reaching up to 7.16 cm^2 V^{-1} s^{-1}, positioning them at the forefront of n-type materials for OFETs.[14] While the continued development of new n-type monomers remains important, significant progress can also be made by reorganizing and modifying existing materials to better leverage their inherent electronic properties for more effective and scalable applications, such as batteries or displays.[15,16] To enable the development of practical, large-scale electronics, it is crucial to use materials that are readily available from affordable commercial sources, which can be easily modified using established protocols, all while maintaining excellent stability. Naphthalene diimide (NDI), perylenediimide (PDI), and benzothiadiazole (BT) cores have emerged as highly promising candidates for wide range of organic electronics applications.[17–19] These cores offer several advantages, including their wide availability from inexpensive commercial sources and their potential for derivatization and expansion. In studying the practical aspects of the double acceptor polymer concept for OFETs, carefully selecting electron-accepting moieties that meet these criteria are important. This approach ensures that the materials chosen are not only compatible with

[a] *Department of Chemical Engineering, Texas A&M University at Qatar, Education City, Doha 23874, Qatar*
[b] *Materials Science and Engineering, Gwangju Institute of Science and Technology (GIST), Gwangju, Korea*
[c] *Vinča Institute of Nuclear Sciences – National Institute of the Republic of Serbia, University of Belgrade, Centre of Excellence for Photoconversion, P.O. Box 522, 11001 Belgrade, Serbia*
[d] *Department of Chemistry, Texas A&M University, College Station, USA*
[e] *College of Science and Engineering Hamad Bin Khalifa University, Education City, Doha 34110, Qatar. E-mail: malhashimi@hbku.edu.qa*
[f] *Hamad Bin Khalifa University, Education City, Doha 34110, Qatar*
† S. S. A. and J. H. K. contributed equally.

cost-effective production, and easy modification but also support scalability for large-scale applications. Both NDI and PDI cores exhibit remarkable stability, high electron affinities, and feature planar conjugated bicyclic structures.[20–22] These structural characteristics enhance π–π stacking interactions, resulting in improved performance.[23,24] Notably, PDI-based thin films and single crystals have demonstrated impressive electron mobilities ranging from 1 to 6 $cm^2 V^{-1} s^{-1}$ under vacuum and ambient conditions.[25] On the other hand, NDI-based polymers have gained recognition as high-performance n-type materials, exemplified by commercially available options such as N2200 and its analogues,[26] which have become benchmark standards in the field.[27–29] The performances of NDI-based materials in n-type OFETs have paved for the way for their application in emerging fields like electrochemical transistors and thermoelectrics.[30,31] In addition, BT is commonly used as a strong acceptor moiety core in modern photovoltaic applications and is widely incorporated into high performance OFET materials, including dual and triple acceptor designs.[32–35] Its success is attributed to its high electron affinity, stability, planar structure and ease of synthesis, along versatile modifications such as core expansion and convenient fluorination.[19,36–38] Fluorination, is recognized as an important strategy for enhancing the performance of n-type conjugated polymers.[39] Incorporating fluorine atoms into the polymer backbone can lower both the highest occupied molecular orbital (HOMO) and the lowest unoccupied molecular orbital (LUMO) energy levels, thereby increasing electron affinity and improving charge injection efficiency.[40] This modification also promotes molecular coplanarity and π–π stacking interactions, which are essential for efficient charge transport.[41,42] Therefore, systematically varying the number of fluorine atoms (0, 1, or 2) on the BT core allows for precise tuning of electronic properties and molecular organization, ensuring optimal semiconductor performance.[43] Additionally, incorporating of thiazole (Tz) units into polymer backbones, particularly as a thiophene replacement, further enhances n-type materials by promoting a more coplanar geometry, stronger π–π stacking, and improved electronic performance.[44,45] As an electron-deficient heterocycle, thiazole strengthens electron-accepting properties, enabling better charge transport and unipolar n-type behaviour in OFETs.[22,46–48] However, its high electron deficiency and asymmetric structure complicates C2 bromination, a key step for further developent.[49]

To address this challenge, we employed electron-deficient Tz-TIPS building blocks and developed a one-pot TIPS removal-bromination strategy. This approach simplifies the synthetic step, improving scalability and facilitates access to n-type Tz-based conjugated polymers, advancing next-generation electron-transporting materials.[45,46,50,51]

Results and discussion

Monomer synthesis

The general synthetic route for monomer synthesis is depicted in Scheme 1. Stille coupling of 2-(triisopropylsilyl)-5-(trimethylstannyl)thiazole (**1**) with commercially available NDI-Br_2 (**2**) and PDI-Br_2 (**3**) using $Pd(PPh_3)_4$ as a catalyst afforded thiazole flanked compounds **4** and **5** as a yellow solid in 75% yield and a maroon red solid in 91%, respectively. Attempts to brominate the 2-position of thiazole in compounds **6** and **7** after TIPS deprotection were unsuccessful. Conventional methods,

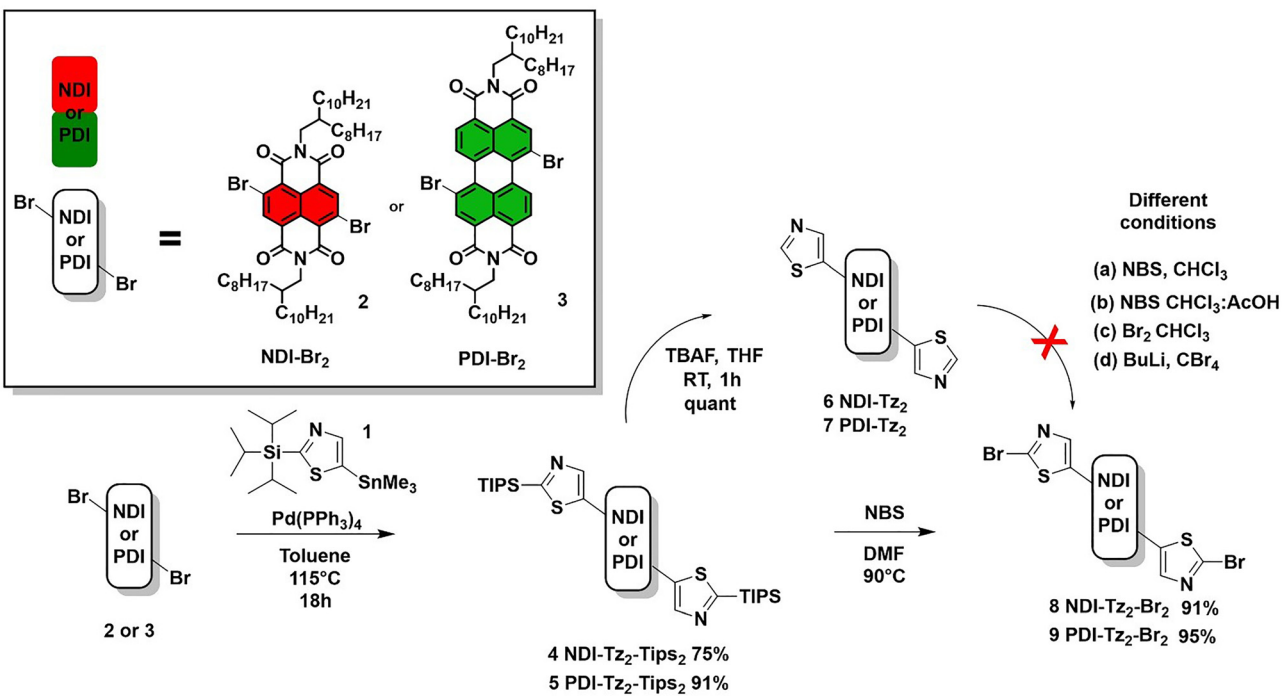

Scheme 1 Synthetic route to thiazole flanked NDI/PDI monomers.

including TBAF-mediated deprotection followed by bromination using *N*-bromosuccinimide (NBS) or bromine (Br_2) under various conditions, failed to produce the desired dibrominated products (Table S1). This challenge likely stems from the highly electron-deficient nature of compounds **6** and **7**. Alternative bromination strategies, such as generating an anion and subsequently reacting with CBr_4 also led to undesired ring-opened imides. Trimethylsilyl (TMS) protected thiophenes and selenophenes are known to undergo direct bromination at the 2-position using NBS in acetic acid.[52,53] However, direct bromination of TIPS-protected thiazoles has not been previously reported. Thus, efforts were undertaken to investigate the direct one-pot bromination of compounds **4** and **5**. After optimization studies, we found that the bromination using NBS 6 equiv. in DMF at 90 °C proceeded smoothly affording >90% yield in just 30 minutes.

To further explore this approach, was applied the optimized protocol to a range of electron deficient TIPS-protected precursors, systemically varying the electronic properties of the thiazole substrate (Schemes S1–S6). As depicted in Fig. 1, the precursors underwent efficient dibromination using this one pot strategy (NBS/DMF). The resulting products either precipitated upon cooling or were re-crystallized, affording the pure products **M1–M6** in good to excellent yields. All the precursors and monomers were characterized by NMR spectroscopy (Fig. S1–S38), while single crystal XRD analysis of M1 is reported in Fig. S39 and Tables S2–S7. Silicon hypervalency and its strong coordination ability with Lewis basic solvents such as DMF, NMP, and HMPA are well documented.[54–57] Over the years, this phenomenon has evolved into a powerful synthetic tool in organic and material chemistry, enabling new strategies for bond activation and selective transformations.[58]

This observation led us to rationalize the process as a silicon-assisted halogenation pathway facilitated by DMF coordination. At elevated temperatures, DMF interacts with the TIPS protecting group *via* hypervalency, promoting concerted deprotection and *in situ* bromination at the C2-thiazole site, as depicted in Scheme 2. Initially, anhydrous DMF coordinates with the TIPS group, forming a hypervalent silicon species **3b**. This coordination weakens the C2–Si bond, leading to bond elongation and destabilization. At elevated temperatures (90–100 °C), this bond becomes sufficiently destabilized, enabling the formation of a highly nucleophilic thiazolyl anion or a transient polarized intermediate **3b**. This activated species then undergoes selective electrophilic bromination at C2 *via* reaction with NBS. Finally, eliminating the silyl group yielding the C2-dibrominated thiazole product **3d**.

The proposed mechanism is supported by three key experimental observations and NMR spectroscopic comparison of TIPS-protected and deprotected intermediates. First, the reaction proceeds cleanly only in anhydrous DMF, indicating the involvement of an ionic intermediate that is highly sensitive to moisture. Second, the highest yields are obtained for highly electron-deficient systems, which stabilize the thiazolyl anionic species, enhancing its reactivity toward bromination. Finally, the reaction requires elevated temperatures (90–100 °C), which are necessary to destabilize the C2–Si bond, allowing its elongation and eventual cleavage to generate the reactive nucleophilic intermediate. Notably, conventional methods for TIPS deprotection and bromination fail to achieve selective functionalization under similar conditions, highlighting the uniqueness of this solvent-mediated, thermally activated pathway. These observations collectively support an ionic mechanism in which solvent coordination, thermal activation, and electronic effects govern the selective bromination of the thiazole ring. Further insight is gained from ^{13}C NMR analysis of the

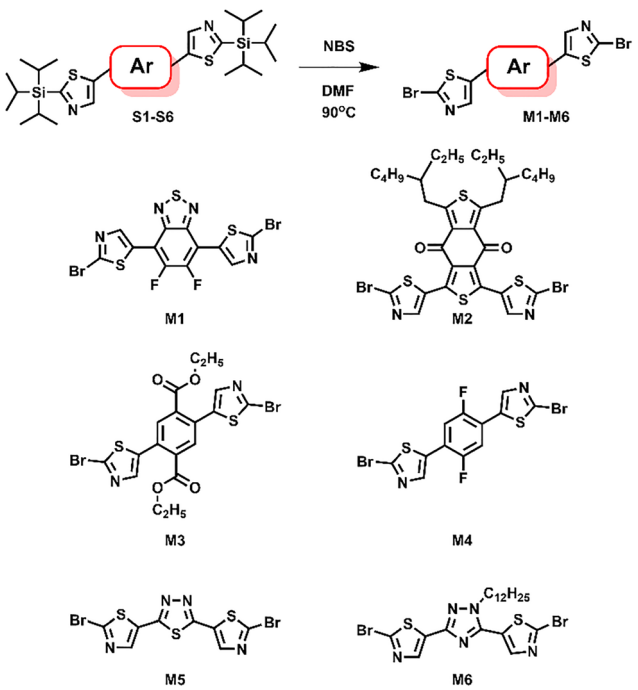

Fig. 1 Structures of heteroaromatic monomers obtained *via* one-pot deprotection and bromination of thiazole C-2 position.

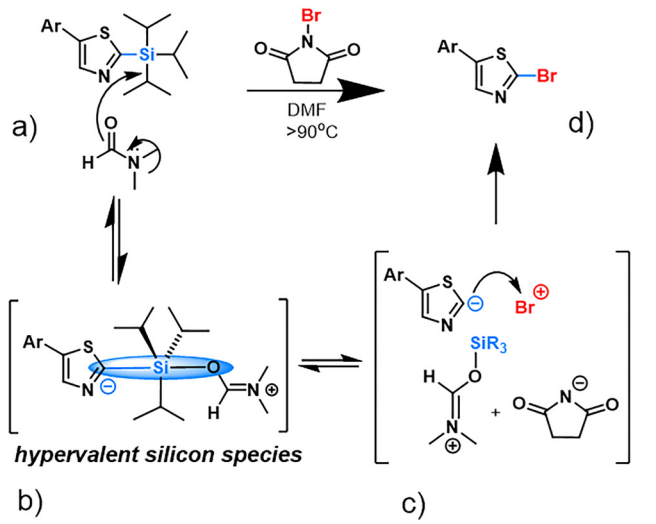

Scheme 2 Postulated mechanism for bromination at the C2 position in Silyl protected thiazole.

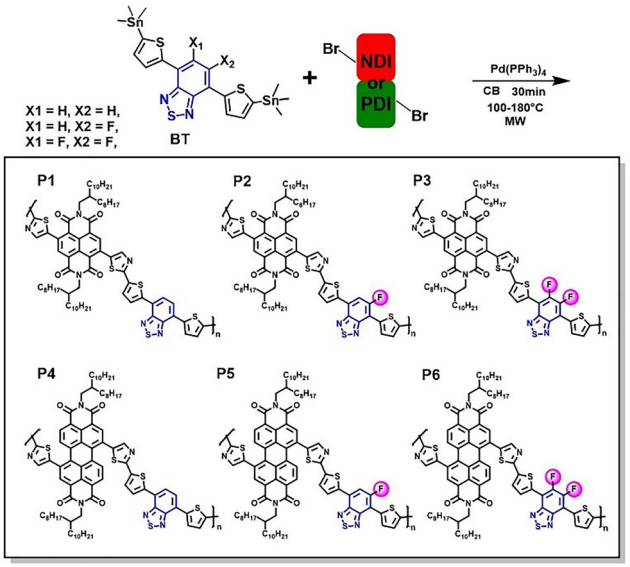

Scheme 3 Synthesis of copolymers **P1–P6**.

2-position carbon of the thiazole ring. In the TIPS-protected compound **4** (TIPS-Tz-NDI-Tz-TIPS), the thiazole 2-carbon resonates downfield at $\delta \sim 172$ ppm, while in the deprotected **6** (Tz-NDI-Tz), it shifts up field to $\delta \sim 162$ ppm. This chemical shift trend suggests reduced electron density in the silylated species, inconsistent with electron-donating hyperconjugation from the silicon group. We propose that this behaviour arises from a combination of inductive electron withdrawal and steric interactions involving the thiazole nitrogen lone pair and the bulky TIPS group. The lone pair on the thiazole nitrogen can repulse the adjacent TIPS group, potentially distorting the geometry and weakening conjugation at the 2-position. This steric and electronic interplay may reduce the activation of the carbon centre toward electrophilic substitution, supporting the case for an alternative, silicon-centered reaction pathway.

Additionally, a solid indication of a hypervalent silicon-based mechanistic pathway is provided by the observation that heating NDI-Tz_2-$TIPS_2$ in dry DMF gradually leads to TIPS deprotection, resulting in the formation of NDI-Tz_2. This transformation occurs in the absence of external electrophiles, supporting the involvement of a thermally induced desilylation process possibly proceeding through a hypervalent silicon intermediate, rather than a classical ipso-substitution mechanism.

Polymer synthesis

Copolymers **P1–P6** were readily synthesised by microwave-assisted palladium Stille coupling between NDI-Tz_2-Br_2 (**8**), and PDI-Tz_2-Br_2 (**9**) and the corresponding non-fluorinated, mono- and di-fluorinated 4,7-bis(5-(trimethylstannyl)thiophen-2-yl)benzo[*c*][1,2,5] thiadiazole BT unit (Scheme 3). To ensure high purity, all copolymers underwent sequential Soxhlet extraction with methanol, acetone and hexane to remove low molecular weight oligomers and catalyst residues. Finally, the chloroform soluble fraction was collected concentrated, and precipitated in methanol to afford the copolymers in moderate yields 40–50%. The number-average molecular weights (M_n) were measured by gel permeation chromatography (GPC) in chlorobenzene at 85 °C using polystyrene standards. All six copolymers **P1–P6** were readily soluble in chloroform, with M_n values ranging from 9–14 KDa and narrow polydispersity index ($Đ$) values between 1.4–1.8. The low molecular weights observed are likely a result of the limited solubility of the growing polymer chains, which leads to early precipitation and termination of polymerization.[45,59] This effect is further intensified by the rigid and planar structures of the NDI and BT units, which tend to aggregate and precipitate from the reaction medium. Additionally, the reduced reactivity of the 2-brominated thiazole unit in cross-coupling polymerization may contribute to restricted chain growth.[60,61]

Polymer optical and electrochemical properties

The optical and electrochemical properties of the copolymers are summarized in Table 1, with Fig. 2 presenting the UV-vis absorption spectra of **P1–P6** in dilute chloroform solutions ($\sim 10^{-5}$ M) and as thin films. The spectra exhibit two distinct absorption bands: a higher-energy band (λ_{max}) attributed to localized electronic transitions of the conjugated units and a lower-energy intramolecular charge transfer (ICT) band, which reflects electron transfer from the donor moieties to the electron-deficient NDI/PDI cores. The optical bandgap (E_g^{opt}) for NDI-Tz-based polymers (**P1–P3**) ranges from 1.55 to 1.61 eV, while PDI-Tz-based polymers (**P4–P6**) exhibit slightly broader bandgaps (1.59–1.73 eV), which are closely aligned with the electrochemical bandgap values (E_g^{EC}) obtained from cyclic

Table 1 Molecular weights, optical and electrochemical properties of **P1–P6**

Polymer	M_n,[a] kg mol^{-1}	$Đ$[b]	λ_{max} solution[c] (nm)	λ_{max}[c] film (nm)	LUMO[d] [eV]	HOMO[d] [eV]	E_g^{opt}[e] [ev]	E_g^{EC}[f] [eV]
P1	14	1.42	502	540	−3.88	−5.67	1.55	1.79
P2	12	1.63	580	599	−4.02	−5.76	1.57	1.74
P3	10	1.38	608	622	−3.98	−5.84	1.61	1.86
P4	13	1.55	500	505	−3.82	−5.77	1.59	1.95
P5	11	1.81	511	515	−3.87	−5.83	1.63	1.96
P6	9	1.73	520	519	−3.91	−5.85	1.73	1.94

[a] Determined by GPC using polystyrene standards. [b] $Đ = M_w/M_n$. [c] λ_{max} in a chloroform solution and as a thin film spin coated from chloroform solution on quartz. [d] Electrochemical $E_{HOMO}/E_{LUMO} = E_{onset(Fc/Fc^+ vs.\ Ag/Ag^+)} - E_{onset} - 4.8$, where 4.8 eV is the ferrocene energy level below the vacuum level and $E_{onset(Fc/Fc^+ vs.\ Ag/Ag^+)} = 0.46$ V. [e] Electrochemical band gap $E_g^{EC} = E_{HOMO} - E_{LUMO}$. [f] Optical $E_{LUMO}^{opt} = E_{HOMO} + E_g^{opt\ film}$.

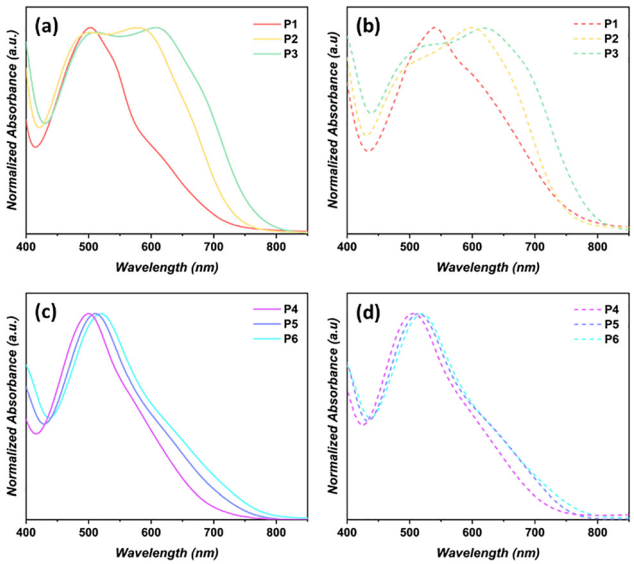

Fig. 2 Normalized UV-vis absorption spectra of copolymers in dilute ($\sim 10^{-5}$ M) chloroform solution and thin-film state. (a), (b) NDI-based copolymers (**P1–P3**) in solution and film, respectively. (c), (d) PDI-based copolymers (**P4–P6**) in solution and film, respectively.

voltammetry (Fig. 3). The introduction of fluorine atoms at the benzothiadiazole (BT) core does not significantly alter the HOMO–LUMO energy levels, indicating that all copolymers are inherently electron-deficient enough that fluorine substitution does not drastically shift their frontier molecular orbitals (Fig. 3). However, cyclic voltammetry data confirm that all copolymers (**P1–P6**) exhibit distinct reduction waves, consistent with their unipolar n-type characteristics. Fluorination leads to more pronounced reduction peaks with weaker oxidation waves, suggesting an enhancement in n-type behavior. The presence of fluorinated substituents influences multiple aspects of π-conjugated polymers, including electronic structure, molecular packing, optical properties, and charge transport.[38,39,42,62]

Analysis of UV-vis spectra in both solution and thin-film states reveal how fluorination in tandem with backbone structure modulate the optoelectronic behavior of the polymers. UV-vis spectra in both solution and thin-film states reveal how backbone identity and fluorination pattern shape optoelectronic properties across the NDI and PDI series. In the NDI-based polymers (**P1–P3**), increasing fluorine content leads to a progressive red shift from 502 to 608 nm in solution and 540 to 622 nm in films, indicating enhanced intramolecular ICT and extended conjugation. These effects are amplified in the solid state, suggesting additional aggregation-induced ordering, especially in **P3**. However, the intermediate mono-fluorinated **P2** shows less crystallinity by GIWAXS and lower mobility than **P3**, suggesting that asymmetric fluorination introduces torsional strain and disrupts molecular planarity. In contrast, the di-fluorinated **P3**, with symmetric substitution, exhibits sharp GIWAXS features, the most red-shifted absorption, and the highest electron mobility in the series. This underscores the importance of symmetry in promoting coplanarity and effective π–π stacking, consistent with prior reports that asymmetrically fluorinated NDI polymers suffer from conformational disorder, while symmetric fluorination enhances ordering and charge transport.[24,63] In the PDI-based series (**P4–P6**), fluorination induces weaker and more irregular spectral shifts: in solution increasing slightly from 500 nm (**P4**) to 511 nm (**P5**), but blue-shifting to 506 nm in **P6**. This non-monotonic trend is even more pronounced in the film spectra: 505 nm (**P4**) → 515 nm (**P5**) → down to 519 nm (**P6**). This reversal upon di-fluorination suggests that fluorination and the bulky PDI core act in conflict: while fluorine attempts to induce planarity and ICT, PDI's steric demands resist these adjustments, leading to torsional distortion and conjugation breakdown. GIWAXS supports this: **P4** and **P5** show comparable, modest crystallinity, while **P6** exhibits weaker and broader diffraction peaks, reflecting structural disruption. Notably, **P6** also shows the lowest electron mobility across all polymers. These trends confirm that fluorination alone does not enhance ordering in PDI-based polymers, and may in fact be detrimental at higher levels due to incompatibility between fluorine-induced interactions and PDI's rigid geometry.[38,63] These results underscore the importance of aligning fluorination patterns with backbone geometry to fine-tune electronic structure, molecular organization, and charge transport in n-type semiconductors.

Thermal properties

The thermal properties of copolymers **P1–P6** were evaluated using thermogravimetric analysis (TGA) and differential scanning calorimetry (DSC), as shown in Fig. S40 and S41. The TGA

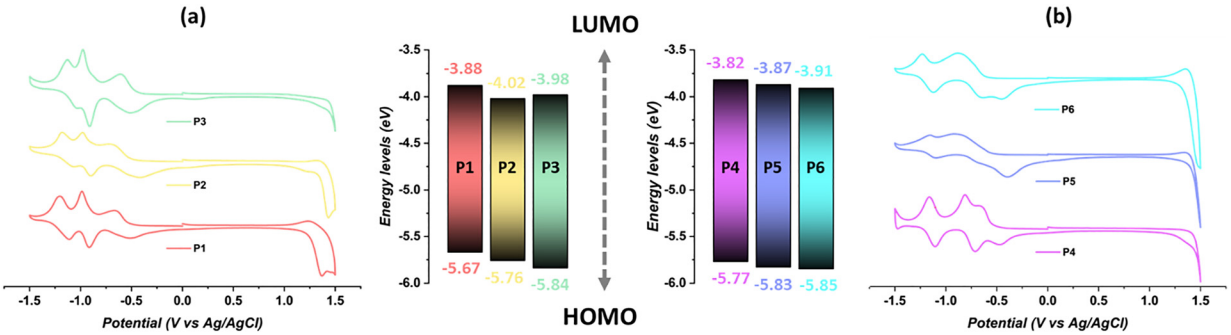

Fig. 3 Cyclic voltammograms and corresponding HOMO–LUMO energy levels of the polymers (a) NDI polymers (b) PDI polymers.

curves indicate that all copolymers exhibit high thermal stability under a nitrogen atmosphere, with high degradation temperatures (T_d) of 200–300 °C as determined by a 5% weight loss when heated at a rate of 10 °C min^{-1}.

DFT-computation

To examine the electronic and optical properties of PDI-Tz-BT and NDI-Tz-BT-based conjugated copolymers, numerical calculations were carried out on **P1** and **P4**, employing density functional theory (DFT) and the time-dependent DFT (TD-DFT), utilizing the Gaussian 09 suit of programs.[64] The ground-state (S0) geometry optimizations of the polymeric structures were performed, within the periodic boundary conditions (PBC), by using the B3LYP functional,[65,66] in combination with the valence double-ζ polarized 6-31G (d,p) basis set.[67] In order to reduce the computational burden, the alkyl side chains from the diimide units were replaced with the methyl groups, for all copolymers. It has been shown that such strategy of reducing the long-chain alkyl groups to methyl groups does not affect the electron distributions and thereby the energy of HOMO/LUMO orbitals, but it could affect the planarity of the system, to some extent.[68] The optimized geometries for two copolymers **P1** and **P4** with the assigned torsion angles between adjacent units are presented in Fig. 4. The structures of the two copolymers are not planar but rather convoluted, because of the steric hindrance between the H-atoms of adjacent Tz units with the oxygen and hydrogen atoms of NDI and PDI cores, respectively. This is consistent with the reported data for the torsion angles between building blocks of polymers containing a thiophene-NDI-thiophene (Th-NDI-Th) sequence,[69–72] whereas a higher degree of planarity is achieved by the coordination of thiazole units *via* the C2-carbon atoms to the NDI core (Tz-NDI-Tz).[71] The spatial electron distribution of the HOMO and LUMO orbitals, placed over the single repeating units of two copolymers, are presented in the lower part of Fig. 4. The analysis shows that the HOMO orbitals of both polymers are fully delocalized over the π-conjugated system of Tz-T-BT-T-Tz sequence, while the LUMO orbitals are placed onto the NDI and PDI aromatic cores. Neither orbital exhibit contributions from the methyl groups, which justifies the strategy of reducing the respective long alkyl chains, in favour of decreasing the computational load. Theoretically predicted band gaps of both copolymers are in excellent agreement with the experimentally determined values by the CV measurements. The calculated bandgap of polymer **P4** is 1.95 eV, which coincides with the experimentally determined value, whereas the HOMO (−5.54 eV) and LUMO (−3.59 eV) levels are both shifted to the less negative potentials by 0.23 eV with respect to the CV results (Table 1). On the other hand, the calculated bandgap of polymer **P1** is 1.82 eV, which is only 0.03 eV overestimated, as compared to the experimental value (1.82 *vs.* 1.79 eV). Theoretically predicted HOMO/LUMO (−5.39/−3.57 eV) levels are located at the more positive potentials relative to the CV data for about 0.3 eV (Table 1).

Grazing incidence wide-angle X-ray scattering (GIWAXS)

The molecular packing and crystallinity of the polymer films were investigated using grazing incidence wide-angle X-ray scattering (GIWAXS), with the two-dimensional scattering patterns and corresponding intensity profiles presented in Fig. 5.

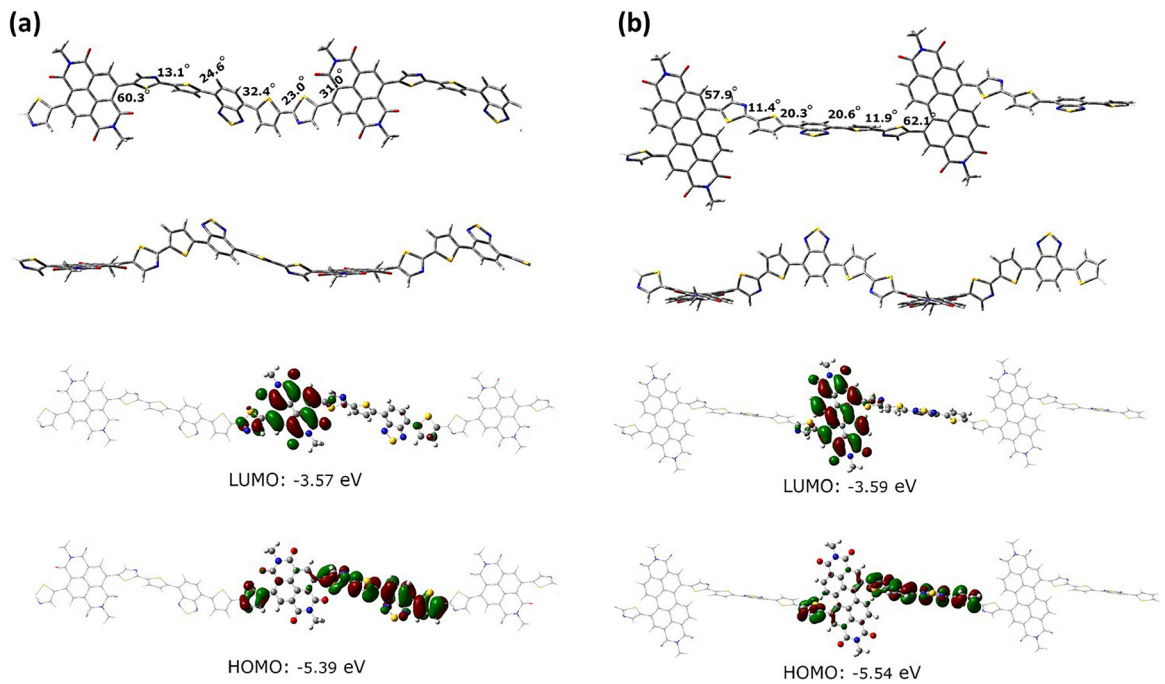

Fig. 4 Representative examples of optimized ground-state structures of copolymers **P1** and **P4** as calculated at the B3LYP/6-31G(d,p) level of theory, with the periodic boundary conditions (PBC). For clarity the HOMO and LUMO orbitals are graphically presented over the single repeat unit.

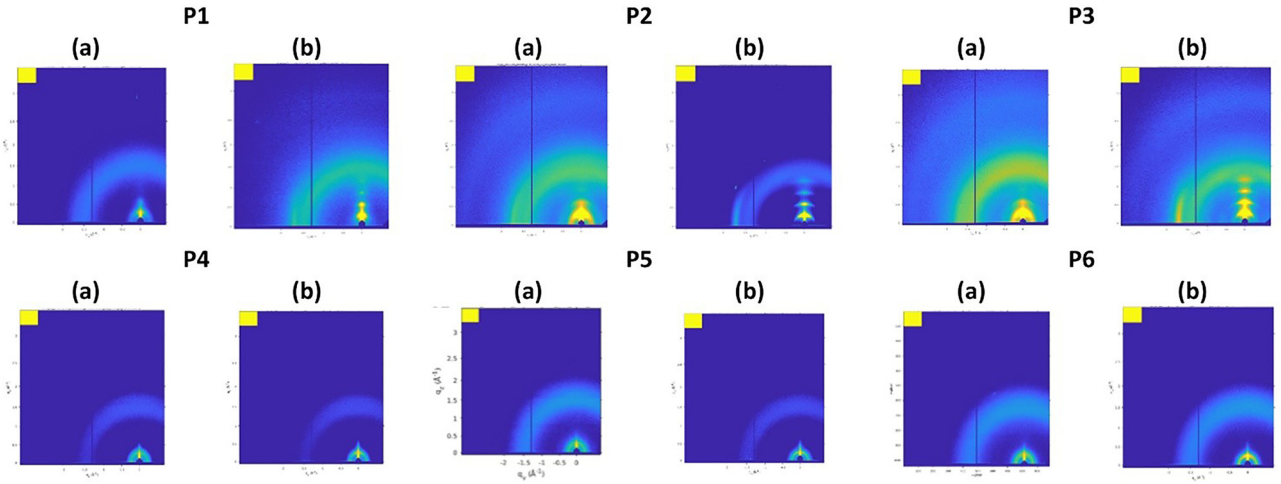

Fig. 5 GIWAXS patterns of **P1–P6** films deposited on silicon wafer substrates (a) as cast (b) annealed films.

Polymer films were spin-coated from 5 mg mL^{-1} chloroform solutions onto Si wafers and annealed at 160 °C for 2 hours in a nitrogen-filled glovebox to enhance molecular ordering. GIWAXS measurements were conducted under vacuum at the Advanced Photon Source, Beamline 8-ID-E (11 keV, incident angle 0.15°).

As-cast films exhibited broad scattering halos and weak out-of-plane lamellar stacking peaks, consistent with a predominantly amorphous morphology, corroborated by DSC measurements showing no discernible thermal transitions. Upon annealing, however, a distinct trend emerged: the NDI-based polymers (**P1–P3**) demonstrated progressively enhanced molecular ordering with increased fluorination. **P2** (mono-fluorinated) and **P3** (di-fluorinated) exhibited sharper out-of-plane lamellar diffraction and more defined in-plane π–π stacking, indicating improved backbone alignment and interchain packing. This enhancement is attributed to the incorporation of fluorine atoms, which promote planarization of the polymer backbone and introduce favorable non-covalent interactions, such as F···H and F···S contacts, facilitating tighter packing.[38]

In contrast, the PDI-based polymers (**P4–P6**) displayed a more nuanced response to fluorination. While **P5** (mono-fluorinated) showed a modest improvement in packing order over **P4** (non-fluorinated), further fluorination in **P6** resulted in broader, less defined diffraction features. This reduced ordering can be rationalized by the intrinsic structural characteristics of the PDI core. Unlike the smaller and more flexible NDI unit, the PDI moiety is larger, more rigid, and sterically congested, which limits its ability to accommodate backbone adjustments induced by fluorination. Excessive fluorination in such fused-ring systems can introduce local distortions or steric clashes that counteract the expected packing benefits, as supported by previous reports that highlight how rigid PDI systems may suffer from reduced crystallinity and film uniformity upon over-fluorination.[73] In NDI-based systems, annealing significantly enhances crystallinity, as seen in Fig. 5. **P2** and **P3** display sharper out-of-plane lamellar and in-plane π–π stacking features, indicating improved molecular order and edge-on orientation. Their scattering profiles show distinct lamellar peaks in the out-of-plane direction and π–π stacking features in-plane, suggesting a predominantly edge-on orientation of the polymer backbones relative to the substrate. This packing geometry is known to support effective charge transport in OFETs and is consistent with the enhanced mobilities observed in these two polymers. Among the NDI based polymers, **P3** shows the sharpest features and the highest electron mobility, which we attribute to fluorination-induced backbone planarity and denser packing. Such effects of fluorination on molecular ordering have been reported in similar donor–acceptor copolymer systems.[74] In contrast, PDI-based analogues (**P4–P6**) exhibit broader and more diffuse GIWAXS features, indicating lower crystallinity or mixed molecular orientation. This behaviour likely results from steric congestion at the PDI core, particularly upon fluorination, as observed in other rigid acceptor-containing polymers.[75] These structural trends correlate well with the observed charge transport properties.

Atomic force microscopy (AFM)

AFM was carried out on spin-coated, annealed thin films of **P1–P6**, and the height, phase, and 3D topography images are shown in Fig. 6. The tapping-mode AFM images (1 × 1 μm^2) reveal clear differences in the surface morphology of the NDI and PDI based polymer films. The NDI based polymers **P1–P3** shows topographically uniform, feature-poor surfaces with sub-nanometre roughness, trending slightly downward with fluorination (**P1**: R_q = 0.535 nm; **P2**: 0.511 nm; **P3**: 0.479 nm). Together with GIWAXS, where the NDI series gains crystallinity upon annealing and **P3** exhibits the sharpest features, this supports that fluorination tightens packing without introducing surface texturing, consistent with the observed mobility increase **P1** < **P2** < **P3**. Fluorinating the BT unit in NDI copolymers has been reported to lower AFM roughness (~3.0 → ~1.5 nm after annealing) and boost μ_e (NDI–FBT *vs.* NDI–BT),[74] consistent with broad trends reviewed for

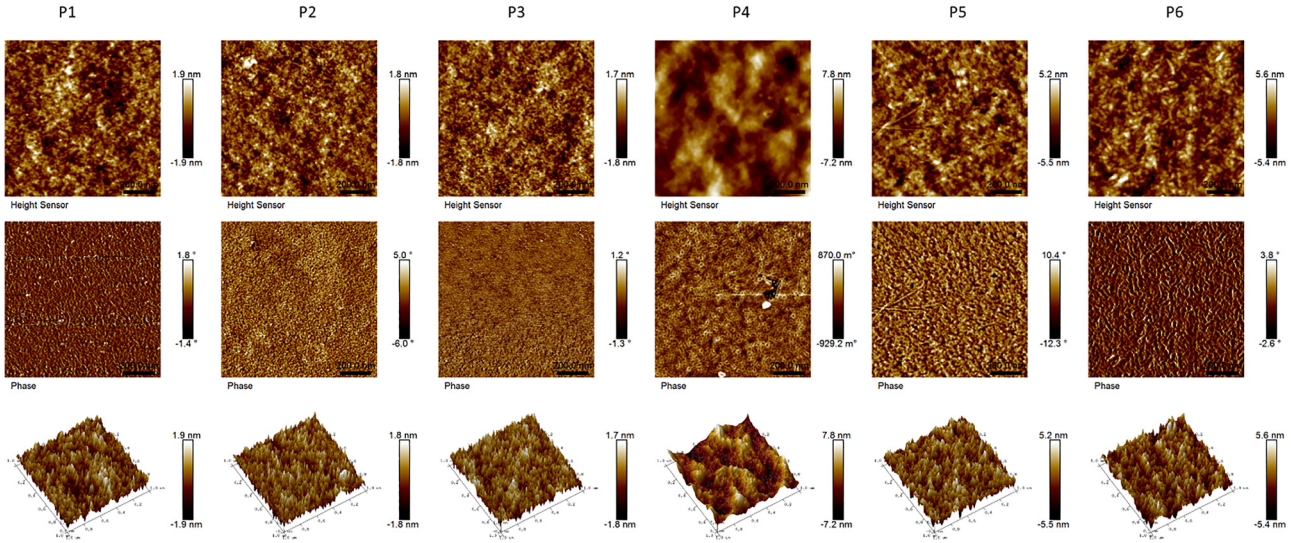

Fig. 6 Atomic Force Microscopy (AFM) tapping mode images recorded over a scan area of 1 × 1 μm^2 of thin films of **P1–P6** showing topography (height sensor, top row), phase (middle row), and corresponding 3D height profiles (bottom row).

fluorinated conjugated polymers.[39] On the contrary for the PDI polymers (**P4–P6**) AFM roughness remains relatively high for the non-fluorinated polymer (P4: $R_q \approx 2.1$ nm) and shows only a modest decrease upon introducing one or two F atoms on the BT unit (**P5–P6**: $R_q \approx 1.5$–1.6 nm). This aligns with broadened GIWAXS features and a monotonic decline in μ_e, indicating that added fluorine exacerbates steric congestion and packing mismatch around the bay-crowded PDI core.[76] Comparable $R_q \approx$ 1–2 nm values are widely reported for PDI-based films, and GIWAXS/AFM studies that deliberately tune bay-site sterics show that film morphology and crystalline order are governed primarily by the bulky PDI bay crowding.

Charge transport and OFET performance of polymers P1–P6

The charge transport properties of thiazole-flanked NDI/PDI-based polymers were analyzed in bottom-gate/bottom-contact (BG/BC) organic thin-film transistors (OTFTs) (Fig. 6). The devices were fabricated on SiO_2 (300 nm)/p^{++}-Si substrates, where gold (Au) and chrome (Cr) contacts were thermally evaporated using a shadow mask, followed by octadecyltrimethoxysilane (OTS) treatment. (Fig. S42) Polymer films were spin-coated from 5 mg mL^{-1} chloroform solutions, annealed at 200 °C for 10 min in an N_2-filled glovebox, and characterized under vacuum. Further details on the fabrication process are provided in the SI. To optimize OTFT performance, we investigated the effects of annealing temperature, electrode materials, and device configuration. It was found that gold (Au) contacts exhibited higher electron mobility (μ_e) than aluminum (Al) contacts, which is attributed to a redox reaction between Al and the n-type semiconductor, leading to a higher injection barrier.[8,77] Despite the relatively large energy barrier (~1 eV) between Au and the n-type semiconductor, the redox-induced injection barrier with Al further hinders electron transport, ultimately lowering μ_e. Additionally, higher annealing temperatures and shorter annealing times promoted better charge transport, as confirmed by GIWAXS analysis, which showed improved molecular ordering upon annealing (Fig. 5). Degree of fluorination plays a critical role in tuning the electronic structure, molecular packing, and charge transport properties of the reported polymers. All polymers displayed unipolar n-type transport behavior with negligible hole current under negative gate bias ($V_g = -60$ V), consistent with their deep LUMO levels estimated from cyclic voltammetry (Fig. 3). Among the NDI-based polymers, fluorine substitution systematically increased μ_e, as **P1**, the non-fluorinated polymer, exhibited an average μ_e of 1.0×10^{-4} cm^2 V^{-1} s^{-1}, while **P2** and **P3**, featuring mono- and di-fluorination, showed improved μ_e values of 2.2×10^{-4} cm^2 V^{-1} s^{-1} and 2.7×10^{-4} cm^2 V^{-1} s^{-1}, respectively. This enhancement is attributed to fluorine's strong electron-withdrawing nature, which lowers the LUMO energy level, improving electron injection and transport efficiency. This correlation is further supported by cyclic voltammetry results, where **P2** and **P3** exhibit lower LUMO levels, in agreement with previous studies. Additionally, GIWAXS data confirm that fluorinated polymers exhibit increased crystallinity after annealing (Fig. 5), further contributing to enhanced charge transport by reducing energetic disorder and improving π–π stacking. In contrast to the NDI-based polymers, PDI-based analogs exhibited a different trend in response to fluorination and charge transport. While non-fluorinated **P4** demonstrated the highest mobility (9.8×10^{-4} cm^2 V^{-1} s^{-1}) among PDI-based polymers, exceeding that of most NDI-based counterparts, fluorination unexpectedly led to a decrease in electron mobility. The μ_e values of monofluorinated **P5** and difluorinated **P6** declined to 4.8×10^{-4} cm^2 V^{-1} s^{-1} and 2.4×10^{-4} cm^2 V^{-1} s^{-1}, respectively. Although fluorine substitution effectively lowers the LUMO level, GIWAXS analysis revealed that crystallinity did not significantly improve in PDI polymers upon fluorination (Fig. 6). Instead, fluorine may disrupt molecular arrangement, leading to rougher film morphology and weaker interchain

Table 2 Summary of the OFET electron mobilities for copolymers **P1–P6**

Polymer	μ_e[a] ($cm^2\ V^{-1}\ s^{-1}$)	V_{th}[b] (V)	I_{on}/I_{off}
P1	1.0×10^{-4} (1.6×10^{-4})	20	10^2–10^3
P2	2.2×10^{-4} (3.0×10^{-4})	28	10^2–10^3
P3	2.7×10^{-4} (3.9×10^{-4})	22	10^3–10^4
P4	9.8×10^{-4} (1.3×10^{-3})	9.3	10^3–10^4
P5	4.8×10^{-4} (7.6×10^{-4})	3.2	10^3–10^4
P6	2.4×10^{-4} (3.1×10^{-4})	12	10^2–10^3

[a] Average mobility values from at least 10 devices with maximum mobilities are shown in parentheses, and the mobility values are extracted based on the average slope from 40 to 50 V in the $I^{1/2}$ *vs.* V plots. [b] Average threshold values are shown.

interactions, thereby reducing transport efficiency. The threshold voltage (V_{th}) of the NDI-based polymers ranged from 9.3 V to 28 V (Table 2). The use of OTS-based Self-assembled monolayers (SAMs) generally increased V_{th} and lowered the on/off ratio, while employing amine-based SAMs may further optimize OTFT performance (Fig. 7).

The output curves suggest that contact resistance still exists, even with noble Au electrodes, indicating that further interfacial engineering is necessary to reduce parasitic resistance and enhance charge injection efficiency. These findings highlight the importance of balancing electronic structure, molecular packing, and processing conditions to optimize charge transport in n-type semiconducting polymers.

The moderate electron mobilities of **P1–P6**, compared to benchmark NDI- and PDI-based polymers, stem from multiple factors. Low M_n (9–14 kDa) due to early chain precipitation limits interchain coupling. The 2-brominated thiazole units show reduced reactivity, possibly introducing defects. While fluorination improves planarity in NDI-based systems, GIWAXS shows poor crystallinity in PDI analogs, especially **P6**. DFT results indicate torsional strain and nonplanar backbones. Contact resistance in the BG/BC device setup may also suppress mobility. These factors collectively explain the performance gap and highlight areas for further optimization.

Conclusions

2-Bromo-thiazole-flanked NDI and PDI monomers were synthesized using an unconventional direct bromination method, employing TIPS-protected thiazoles as starting materials. This synthetic strategy, which avoids the need for traditional bromination techniques, was successfully demonstrated through a series of examples, confirming its efficacy and reliability. The electronic properties of the thiazole-flanked NDI and PDI-based copolymers were thoroughly investigated using both cyclic voltammetry and DFT calculations. The DFT results reveal that the NDI/PDI-Tz core architecture allows for an effective extension of conjugation within the NDI–bridge–NDI system, if steric hindrance does not disrupt the planarity of the polymer backbone. This extension of conjugation is critical for enhancing charge transport properties in electronic devices. Furthermore, the electron mobilities of the solution-processed

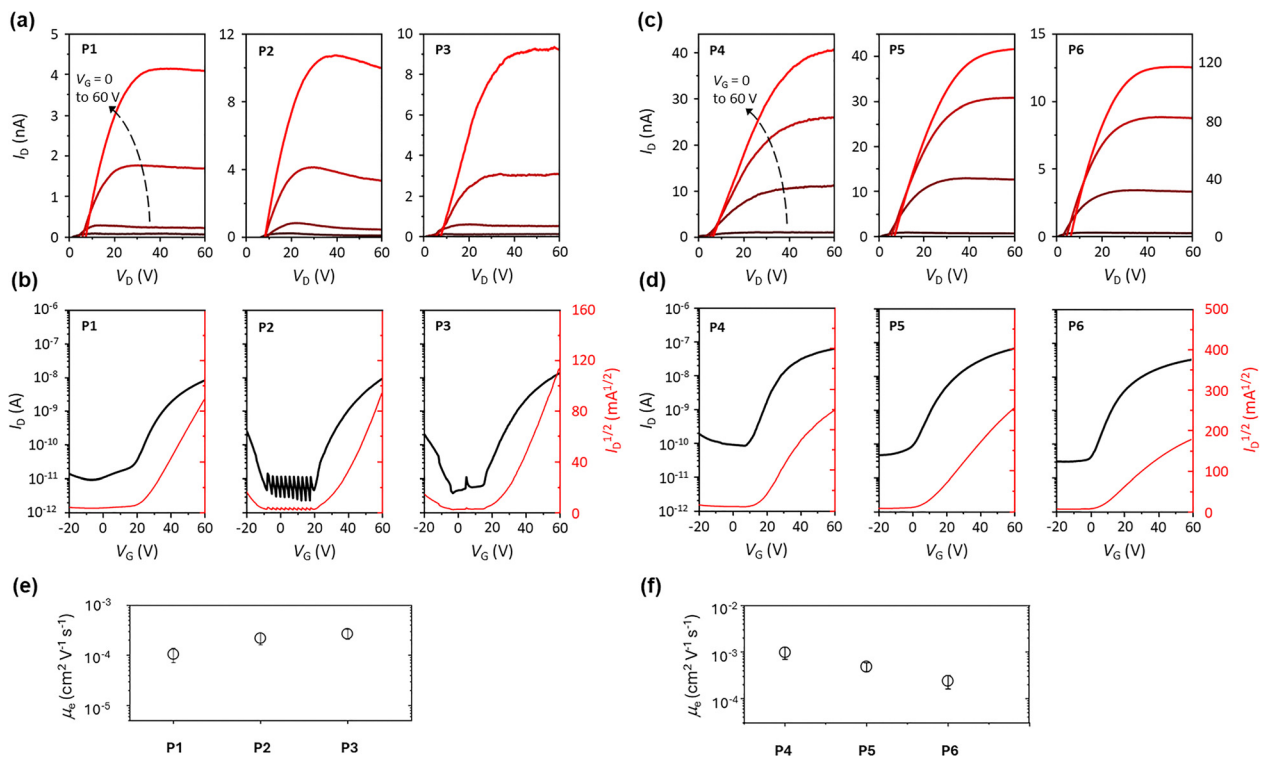

Fig. 7 Transfer (a) & (c) and output (b) & (d) characteristics of OTFTs of polymers **P1–P6** and comparative electron mobility chart of NDI based copolymers (e) and PDI based copolymers (f).

NDI/PDI-based polymers, ranging from 1.3×10^{-3} to 4.8×10^{-4} cm^2 V^{-1} s^{-1}, were found to be comparable to those of other semiconductors with similar structural characteristics. These values highlight the potential of thiazole-flanked NDI and PDI copolymers as effective candidates for use in organic electronic applications, such as field-effect transistors.

Author contributions

The manuscript was written through contribution of all authors. All authors have given approval to the final version of the manuscript.

Conflicts of interest

The authors declare no conflict of interest.

Data availability

The datasets supporting this study are openly available in the supplementary information (SI). See DOI: **https://doi.org/10.1039/d5ma00573f**.

Acknowledgements

M. A acknowledges support from the Qatar Research, Development and Innovation Council, Qatar National Research Fund (ARG01-0522-230270).

Notes and references

1 J. Duan, G. Zhu, L. Lan, J. Chen, X. Zhu, C. Chen, Y. Yu, H. Liao, Z. Li, I. McCulloch and W. Yue, *Angew. Chem., Int. Ed.*, 2023, **62**, e202213737.
2 C. Gu, X. Su, Y. Li, B. Liu, Y. Tian, W. Tan, J. Ma and X. Bao, *Mol. Syst. Des. Eng.*, 2022, **7**, 1364–1384.
3 H. Jia and T. Lei, *J. Mater. Chem. C*, 2019, **7**, 12809–12821.
4 M. Li and Y. Shi, *ChemPlusChem*, 2023, **88**, e202300215.
5 H. Usta, A. Facchetti and T. J. Marks, *Acc. Chem. Res.*, 2011, **44**, 501–510.
6 S. Yu, C. J. Kousseff and C. B. Nielsen, *Synth. Met.*, 2023, **293**, 117295.
7 Y. Zhou, K. Zhang, Z. Chen and H. Zhang, *Materials*, 2023, **16**, 6645.
8 S. Griggs, A. Marks, H. Bristow and I. McCulloch, *J. Mater. Chem. C*, 2021, **9**, 8099–8128.
9 J. T. E. Quinn, J. Zhu, X. Li, J. Wang and Y. Li, *J. Mater. Chem. C*, 2017, **5**, 8654–8681.
10 Y. Sui, Y. Deng, T. Du, Y. Shi and Y. Geng, *Mater. Chem. Front.*, 2019, **3**, 1932–1951.
11 Y. Zhang, Y. Wang, C. Gao, Z. Ni, X. Zhang, W. Hu and H. Dong, *Chem. Soc. Rev.*, 2023, **52**, 1331–1381.
12 Y. Zhao, Y. Guo and Y. Liu, *Adv. Mater.*, 2013, **25**, 5372–5391.
13 D. Qu, T. Qi and H. Huang, *J. Energy Chem.*, 2021, **59**, 364–387.
14 Y. Wang, T. Hasegawa, H. Matsumoto and T. Michinobu, *J. Am. Chem. Soc.*, 2019, **141**, 3566–3575.
15 J. Chen, S. Wang, S. Ren, R. Meng, W. Shi, M. Zhu, M. Zeng, Y. Zhao, Y. Guo and Y. Liu, *Adv. Funct. Mater.*, 2024, 2418105.
16 A. Innocenti, H. Adenusi and S. Passerini, *InfoMat*, 2023, **5**, e12480.
17 X. Zhan, A. Facchetti, S. Barlow, T. J. Marks, M. A. Ratner, M. R. Wasielewski and S. R. Marder, *Adv. Mater.*, 2011, **23**, 268–284.
18 M. Al Kobaisi, S. V. Bhosale, K. Latham, A. M. Raynor and S. V. Bhosale, *Chem. Rev.*, 2016, **116**, 11685–11796.
19 Y. Wang and T. Michinobu, *J. Mater. Chem. C*, 2016, **4**, 6200–6214.
20 M. Liao, J. Duan, P. A. Peng, J. Zhang and M. Zhou, *RSC Adv.*, 2020, **10**, 41764–41779.
21 R. Matsidik, M. Giorgio, A. Luzio, M. Caironi, H. Komber and M. Sommer, *Eur. J. Org. Chem.*, 2018, 6121–6126.
22 Z. Yuan, C. Buckley, S. Thomas, G. Zhang, I. Bargigia, G. Wang, B. Fu, C. Silva, J.-L. Brédas and E. Reichmanis, *Macromolecules*, 2018, **51**, 7320–7328.
23 S. Gámez-Valenzuela, I. Torres-Moya, A. Sánchez, B. Donoso, J. T. López Navarrete, M. C. Ruiz Delgado, P. Prieto and R. Ponce Ortiz, *Chem. – Eur. J.*, 2023, **29**, e202301639.
24 J. Yang, B. Xiao, K. Tajima, M. Nakano, K. Takimiya, A. Tang and E. Zhou, *Macromolecules*, 2017, **50**, 3179–3185.
25 A. S. Molinari, H. Alves, Z. Chen, A. Facchetti and A. F. Morpurgo, *J. Am. Chem. Soc.*, 2009, **131**, 2462–2463.
26 S. Brixi, O. A. Melville, B. Mirka, Y. He, A. D. Hendsbee, H. Meng, Y. Li and B. H. Lessard, *Sci. Rep.*, 2020, **10**, 4014.
27 M. Kim, W.-T. Park, S. U. Ryu, S. Y. Son, J. Lee, T. J. Shin, Y.-Y. Noh and T. Park, *Chem. Mater.*, 2019, **31**, 4864–4872.
28 Y. Wang, T. Hasegawa, H. Matsumoto, T. Mori and T. Michinobu, *Adv. Funct. Mater.*, 2017, **27**, 1701486.
29 R. Kim, P. S. K. Amegadze, I. Kang, H.-J. Yun, Y.-Y. Noh, S.-K. Kwon and Y.-H. Kim, *Adv. Funct. Mater.*, 2013, **23**, 5719–5727.
30 D. Ohayon, A. Savva, W. Du, B. D. Paulsen, I. Uguz, R. S. Ashraf, J. Rivnay, I. McCulloch and S. Inal, *ACS Appl. Mater. Interfaces*, 2021, **13**, 4253–4266.
31 Y. Song, J. Ding, X. Dai, C. Li, C.-A. Di and D. Zhang, *ACS Mater. Lett.*, 2022, **4**, 521–527.
32 B. Li, X. Zou, Q. Li, H. Sang, Y. Mu, J. Wang, J. Pei, C. Yang, L. Li and X. Wan, *Org. Electron.*, 2023, **113**, 106708.
33 Z. Yi, Y. Jiang, L. Xu, C. Zhong, J. Yang, Q. Wang, J. Xiao, X. Liao, S. Wang, Y. Guo, W. Hu and Y. Liu, *Adv. Mater.*, 2018, **30**, 1801951.
34 G. Kim, A. R. Han, H. R. Lee, J. Lee, J. H. Oh and C. Yang, *Chem. Commun.*, 2014, **50**, 2180–2183.
35 Z. Ni, H. Wang, Q. Zhao, J. Zhang, Z. Wei, H. Dong and W. Hu, *Adv. Mater.*, 2019, **31**, 1806010.
36 B. Nketia-Yawson, H.-S. Lee, D. Seo, Y. Yoon, W.-T. Park, K. Kwak, H. J. Son, B. Kim and Y.-Y. Noh, *Adv. Mater.*, 2015, **27**, 3045–3052.
37 Q. Nie, A. Tang, Q. Guo and E. Zhou, *Nano Energy*, 2021, **87**, 106174.

38 J. Lee, M. Jang, S. M. Lee, D. Yoo, T. J. Shin, J. H. Oh and C. Yang, *ACS Appl. Mater. Interfaces*, 2014, **6**, 20390–20399.
39 T. Zhang, Z. Chen, W. Zhang, L. Wang and G. Yu, *Adv. Mater.*, 2024, **36**, 2403961.
40 Z. Wang, S. Zhu, T. Li, W. Liang, J. Zhou and H. Hu, *ACS Mater. Au*, 2025, **5**, 57–71.
41 A. Zhang, C. Xiao, Y. Wu, C. Li, Y. Ji, L. Li, W. Hu, Z. Wang, W. Ma and W. Li, *Macromolecules*, 2016, **49**, 6431–6438.
42 M. Barłóg, I. Kulai, X. Ji, N. Bhuvanesh, S. Dey, E. P. Sliwinski, H. S. Bazzi, L. Fang and M. Al-Hashimi, *Org. Chem. Front.*, 2019, **6**, 780–790.
43 N. Leclerc, P. Chávez, O. A. Ibraikulov, T. Heiser and P. Lévêque, *Polymers*, 2016, **8**, 11.
44 J. Barron, S. Attar, P. Bhattacharya, P. Yu, M. Al-Hashimi and S. Guha, *J. Mater. Chem. C*, 2022, **10**, 14653–14660.
45 S. Attar, R. Yang, Z. Chen, X. Ji, M. Comí, S. Banerjee, L. Fang, Y. Liu and M. Al-Hashimi, *Chem. Sci.*, 2022, **13**, 12034–12044.
46 L. Zhang, Z. Wang, C. Duan, Z. Wang, Y. Deng, J. Xu, F. Huang and Y. Cao, *Chem. Mater.*, 2018, **30**, 8343–8351.
47 Z. Chen, D. Gao, J. Huang, Z. Mao, W. Zhang and G. Yu, *ACS Appl. Mater. Interfaces*, 2016, **8**, 34725–34734.
48 S.-Y. Lv, Q.-Y. Li, B.-W. Li, J.-Y. Wang, Y.-B. Mu, L. Li, J. Pei and X.-B. Wan, *Chin. J. Polym. Sci.*, 2022, **40**, 1131–1140.
49 E. J. Uzelac and S. C. Rasmussen, *J. Org. Chem.*, 2017, **82**, 5947–5951.
50 Y. Teshima, M. Saito, T. Fukuhara, T. Mikie, K. Komeyama, H. Yoshida, H. Ohkita and I. Osaka, *ACS Appl. Mater. Interfaces*, 2019, **11**, 23410–23416.
51 M. Barłóg, X. Zhang, I. Kulai, D. S. Yang, D. N. Sredojevic, A. Sil, X. Ji, K. S. M. Salih, H. S. Bazzi, H. Bronstein, L. Fang, J. Kim, T. J. Marks, X. Guo and M. Al-Hashimi, *Chem. Mater.*, 2019, **31**, 9488–9496.
52 Q. Zhang, L. Yan, X. Jiao, Z. Peng, S. Liu, J. J. Rech, E. Klump, H. Ade, F. So and W. You, *Chem. Mater.*, 2017, **29**, 5990–6002.
53 Y. Sakamoto, S. Komatsu and T. Suzuki, *J. Am. Chem. Soc.*, 2001, **123**, 4643–4644.
54 S. Rendler and M. Oestreich, *Synthesis*, 2005, 1727–1747.
55 M. Benaglia, S. Guizzetti and L. Pignataro, *Coord. Chem. Rev.*, 2008, **252**, 492–512.
56 S. Kobayashi and K. Nishio, *Tetrahedron Lett.*, 1993, **34**, 3453–3456.
57 S. Kobayashi and K. Nishio, *J. Org. Chem.*, 1994, **59**, 6620–6628.
58 L. M. Wheeler, N. R. Neale, T. Chen and U. R. Kortshagen, *Nat. Commun.*, 2013, **4**, 2197.
59 H.-L. Su, D. N. Sredojevic, H. Bronstein, T. J. Marks, B. C. Schroeder and M. Al-Hashimi, *Macromol. Rapid Commun.*, 2017, **38**, 1600610.
60 X. Xue, C. Li, K. Chenchai, X. Zhang, T. Shi, X. Zhang, G. Zhang and D. Zhang, *Macromol. Rapid Commun.*, 2025, 2500289.
61 S. Wang, H. Sun, T. Erdmann, G. Wang, D. Fazzi, U. Lappan, Y. Puttisong, Z. Chen, M. Berggren, X. Crispin, A. Kiriy, B. Voit, T. J. Marks, S. Fabiano and A. Facchetti, *Adv. Mater.*, 2018, **30**, 1801898.
62 K. Do, Q. Saleem, M. K. Ravva, F. Cruciani, Z. Kan, J. Wolf, M. R. Hansen, P. M. Beaujuge and J.-L. Brédas, *Adv. Mater.*, 2016, **28**, 8197–8205.
63 X. Liu, T. Jin, H. Li, S. Wang, Z. Shen, J. Li, R. Chen, Y. Chen and Y. Han, *Macromolecules*, 2024, **57**, 4141–4157.
64 M. Frisch and F. Clemente, Scalmani, V. Barone, B. Mennucci, G. A. Petersson, H. Nakatsuji, M. Caricato, X. Li, H. P. Hratchian, A. F. Izmaylov, J. Bloino and G. Zhe, Gaussian, 2009, **9**.
65 A. D. Becke, *J. Chem. Phys.*, 1993, **98**, 5648–5652.
66 C. Lee, W. Yang and R. G. Parr, *Phys. Rev. B: Condens. Matter Mater. Phys.*, 1988, **37**, 785.
67 R. Ditchfield, W. J. Hehre and J. A. Pople, *J. Chem. Phys.*, 1971, **54**, 724–728.
68 R. Stalder, C. Grand, J. Subbiah, F. So and J. R. Reynolds, *Polym. Chem.*, 2012, **3**, 89–92.
69 T. Schuettfort, L. Thomsen and C. R. McNeill, *J. Am. Chem. Soc.*, 2013, **135**, 1092–1101.
70 Z. Fei, Y. Han, J. Martin, F. H. Scholes, M. Al-Hashimi, S. Y. AlQaradawi, N. Stingelin, T. D. Anthopoulos and M. Heeney, *Macromolecules*, 2016, **49**, 6384–6393.
71 Z. Yuan, B. Fu, S. Thomas, S. Zhang, G. DeLuca, R. Chang, L. Lopez, C. Fares, G. Zhang, J.-L. Bredas and E. Reichmanis, *Chem. Mater.*, 2016, **28**, 6045–6049.
72 P. Cheng, X. Zhao and X. Zhan, *Acc. Mater. Res.*, 2022, **3**, 309–318.
73 X. Guo, A. Facchetti and T. J. Marks, *Chem. Rev.*, 2014, **114**, 8943–9021.
74 C. An, H. Makowska, B. Hu, R. Duan, W. Pisula, T. Marszalek and M. Baumgarten, *RSC Adv.*, 2018, **8**, 16464–16469.
75 Z. Li, D. Li, Y. Bao, P. Guo, Z. Liang, C. Yang and J. Tong, *Opt. Mater.*, 2025, **162**, 116932.
76 S. R. Suranagi, R. Singh, J.-H. Kim, M. Kim, H. Ade and K. Cho, *Org. Electron.*, 2018, **58**, 222–230.
77 C. V. Hoven, R. Yang, A. Garcia, V. Crockett, A. J. Heeger, G. C. Bazan and T.-Q. Nguyen, *Proc. Natl. Acad. Sci. U. S. A.*, 2008, **105**, 12730–12735.